

# The Wiedemann-Franz law in doped Mott insulators without quasiparticles

Wen O. Wang,<sup>1,2,\*</sup> Jixun K. Ding,<sup>1,2</sup> Yoni Schattner,<sup>2,3</sup> Edwin W. Huang,<sup>4</sup>  
Brian Moritz,<sup>2</sup> Thomas P. Devereaux,<sup>2,5,†</sup>

<sup>1</sup>Department of Applied Physics, Stanford University, Stanford, CA 94305, USA

<sup>2</sup>Stanford Institute for Materials and Energy Sciences, SLAC National Accelerator Laboratory,  
2575 Sand Hill Road, Menlo Park, CA 94025, USA

<sup>3</sup>Department of Physics, Stanford University, Stanford, CA 94305, USA

<sup>4</sup>Department of Physics and Institute of Condensed Matter Theory,  
University of Illinois at Urbana-Champaign, Urbana, IL 61801, USA

<sup>5</sup>Department of Materials Science and Engineering, Stanford University, Stanford, CA 94305, USA

\*E-mail: wenwang.physics@gmail.com. †E-mail: tpd@stanford.edu.

August 22, 2022

**Many metallic quantum materials display anomalous transport phenomena violating Fermi liquid and Boltzmann theory. Here, we study transport in the doped Hubbard model and observe a cross-over separating high- and low-temperature behavior in both thermal and charge transport. Distinct from the incoherent behavior at high temperatures, the Lorenz number as  $T \rightarrow 0$  obeys the Wiedemann-Franz law, even in a doped Mott insulator that lacks well-defined quasiparticles. Analyzing contributions to thermal diffusivity, we find that the potential energy strongly affects thermal transport at high temperatures, while at low temperatures, the behavior of both thermal and charge**

**transport is controlled primarily by the electronic kinetic energy. Our result helps to clarify the interpretation of transport experiments beyond Boltzmann theory in non-Fermi liquid strange metals.**

Landau's notion of quasiparticles greatly simplified the language of transport in systems having a macroscopic number of interacting degrees of freedom in terms of "free" objects with renormalized properties that participate in transport via a semi-classical or Boltzmann framework. As such, transport behavior of Fermi liquids is governed solely by kinematic constraints of a Fermi surface and simple collisions between otherwise free particles. Yet in many correlated metals, including the high- $T_c$  cuprates, anomalous transport phenomena have been uncovered that violate these rules: strange metal resistivity that increases linearly with temperature, not saturating as the quasiparticle mean-free-path approaches the lattice spacing (1, 2); inconsistency with Kohler's rule, which governs the scaling behavior of magnetoresistance from Boltzmann theory (3–5); and violations of the Wiedemann-Franz law, which constrains the ratio of thermal to electrical conductivity (6–15).

The ubiquity of such behavior that violates notions of the Fermi liquid has led to tremendous interest in determining how heat and charge currents propagate in systems without the saving grace of quasiparticles (16–19). Analysis of the large body of experimental transport results in correlated materials has been hindered dramatically by the use of an assumed Boltzmann-like theory and reductive conclusions on the nature of transport in terms of Drude-like concepts, which have no validity when quasiparticles are absent. While this greatly amplifies the need for deeper analysis that avoids oversimplifications, there is very little known from exact methods about the nature of transport in strongly interacting systems. Many advanced numerical calculations have focused on characterizing ground state properties (20, 21), but a picture of transport is incomplete without an understanding of the excited states in these materials. Analytical approaches are hampered by the fact that properly evaluating transport involves calculating many

higher order correlation functions, not relying on the simplifying assumptions of quasiparticles and Boltzmann theory, which only punctuates the need for more accurate and precise determinations of transport.

Here, we study the DC longitudinal thermal conductivity  $\kappa$  in the doped 2D  $t$ - $t'$ - $U$  Hubbard model, which exhibits strange metallic electric transport over a wide hole doping  $p$  and temperature  $T$  range (22–25). We evaluate the many-body Kubo formula using the numerically exact, unbiased, and non-perturbative determinant quantum Monte Carlo (DQMC) (26, 27) algorithm and maximum entropy analytic continuation (MaxEnt) (28, 29). We define  $\kappa$  as the linear-response heat current  $\langle \mathbf{J}_Q \rangle$  induced by a parallel temperature gradient,  $\kappa \equiv -\langle J_{Q,x} \rangle / \partial_x T$ , under the condition of zero charge current. Distinct from the incoherent behavior at high temperatures, we observe that the Lorenz number for this doped strange metal has weak doping dependence in the low temperature regime, and approaches the Wiedemann-Franz law prediction as temperature approaches zero, even in the absence of long-lived quasiparticles. Methodological details, including a systematic analysis of finite size and Trotter errors, as well as extensive supporting data, can be found in the Supplementary Materials. For convenience,  $k_B$ ,  $\hbar$ , and charge  $e$  are set to 1 throughout the paper.

The DC longitudinal thermal conductivity  $\kappa$  is shown in Fig. 1(A); and for comparison, the DC longitudinal charge conductivity  $\sigma$  (22) (multiplied by  $T$ ) is shown in Fig. 1(C). The behavior of both  $\kappa$  and  $\sigma$  in the range of temperatures shown here is different from the expected behavior of the Hubbard model in the infinite-temperature limit where  $\kappa \propto 1/T^2$  and  $\sigma \propto 1/T$  (22, 23, 30) (see Fig. S6 in the Supplementary Materials). We observe a cross-over temperature at roughly  $T_{x0} \sim t$ , separating distinct behavior in two regimes for both  $\kappa$  and  $\sigma$ .  $\kappa$  decreases with doping at high temperatures, while it increases with doping at low temperatures. While  $\sigma$  generally increases with doping at all temperatures, the temperature dependence of  $\sigma \times T$  displays kinks, or even non-monotonic behavior, at roughly  $T_{x0}$ . At sufficiently low

temperatures and away from half-filling,  $\kappa/T$  and  $\sigma$  display similar doping and temperature dependence, as shown in Figs. 1(B) and (D).

To further analyze thermal and charge transport in the two temperature regimes, we use the Einstein relations to calculate the thermal diffusivity  $D_Q \equiv \kappa/c_v$  and charge diffusivity  $D \equiv \sigma/\chi$  (22, 31), as shown in Figs. 2(A) and (B), where  $c_v$  is the specific heat and  $\chi$  is the charge compressibility.  $D_Q$  and  $D$  are not strictly independent diffusivities in the heat and charge channels due to non-zero thermoelectric effects. However, in our parameter regime, corrections from such effects are shown to be small (see Fig. S4 in the Supplementary Materials), so that  $D_Q$  and  $D$  are good approximations to the independent diffusivities  $D_{\pm}$ . There is a cross-over temperature where the doping dependence of  $D_Q$  changes, similar to  $\kappa$ ; and in the low temperature regime below  $T_{xo}$ ,  $D_Q$  behaves similarly to  $D$ . As shown in the inset to Fig. 2(B),  $D^{-1}$  displays strange metallic linear-in- $T$  dependence for high doping, consistent with Ref. (22), and non-monotonic temperature dependence for low doping. Neither of these corresponds to the expected  $T^2$  dependence for a Fermi liquid.

To understand the cross-over in  $D_Q$  and why  $D_Q$  and  $D$  behave similarly at low temperatures, we separate  $D_Q$  into kinetic and potential energy components. In the non-interacting limit ( $U = 0$ ) of the Hubbard model, the Hamiltonian consists only of the kinetic energy. The corresponding charge current operator  $\mathbf{J}$  and (kinetic) energy current operator  $\mathbf{J}_K$  are both weighted two-fermion summations of  $n_{\mathbf{k},\sigma}$ , the density operator with momentum  $\mathbf{k}$  and spin  $\sigma$ . The only difference between the two is an additional weighting factor of the bare-band energy  $\epsilon_{\mathbf{k}}$  in  $\mathbf{J}_K$  (see Supplementary Materials). For interacting systems, the charge current operator keeps the same form, but the energy current operator  $\mathbf{J}_E$  now consists of  $\mathbf{J}_K$ , an additional four-fermion term  $\mathbf{J}_P$ , which we call the potential energy current, and corrections proportional to  $\mathbf{J}$ , depending on the explicit form of the interaction (see Supplementary Materials). The heat current  $\mathbf{J}_Q$  contains an additional correction term  $-\mu\mathbf{J}$ , where  $\mu$  is the chemical potential. However,

under the condition of zero charge current ( $\langle \mathbf{J} \rangle = 0$ ), terms proportional to  $\langle \mathbf{J} \rangle$  will not contribute to  $\langle \mathbf{J}_Q \rangle$ , leaving only  $\langle \mathbf{J}_K \rangle$  and  $\langle \mathbf{J}_P \rangle$ . In this way, we separate the thermal conductivity  $\kappa_{P/K} \equiv -\langle J_{P/K,x} \rangle / \partial_x T$  and the thermal diffusivity  $D_Q = D_P + D_K$ , with  $D_{P/K} \equiv \kappa_{P/K} / c_v$ , into potential and kinetic contributions, which are shown in Figs. 2(C) and (D), respectively.

Above  $T_{x0}$ , the potential contribution  $D_P$  dominates over the kinetic contribution  $D_K$ .  $D_P$  decreases with doping, which can be understood intuitively by looking at the operator form of  $\mathbf{J}_P$  (see Supplementary Materials) as a representation of the flow of double occupancies. A lower density of double occupancies leads to a reduced effective “mean-free path”. Therefore,  $D_P$  should decrease with doping as double occupancies are suppressed. While  $D_P$  dominates at high temperatures, it decreases with decreasing temperature as the flow of double occupancies is frozen out.  $D_K$  increases with decreasing temperature and becomes dominant below  $T_{x0}$ . Comparing the operator form of  $\mathbf{J}$  and  $\mathbf{J}_K$ , both being derived solely from the kinetic energy, it becomes clear that the two are related, which is reflected in the similar behavior of  $D$  and  $D_K$ , as shown in Figs. 2(B) and (D). Since  $D_K$  dominates at low temperatures, the thermal diffusivity  $D_Q$  inherits a similar doping and temperature dependence to that of the charge diffusivity  $D$ .

At low temperatures, below  $T_{x0}$ , both the thermal and charge transport are controlled by the kinetic energy. This conclusion can be reinforced by looking at the Lorenz number, the ratio between the thermal and charge transport  $L \equiv \kappa / (T\sigma)$ , as shown in Fig. 3. Aside from half-filling in the Mott insulator, where  $L$  diverges with decreasing temperature, in the doped metals  $L$  displays a similar cross-over at  $\sim T_{x0}$ . Above  $T_{x0}$ ,  $L$  has a non-monotonic temperature dependence and decreases with increasing doping, primarily influenced by the potential energy contributions to thermal transport and the flow of double occupancies. The system lacks long-lived quasiparticles and is comprised of incoherent electrons with extraordinarily short mean-free-paths. Below  $T_{x0}$ ,  $L$  has a weak doping dependence and increases with decreasing temperature. As  $T \rightarrow 0$  for the temperatures that we can access,  $L$  appears to approach

$L_0 \equiv \pi^2/3$  – the Lorenz number predicted by the Wiedemann-Franz law.

As the Wiedemann-Franz law applies only to the asymptotically low-temperature limit, where one can learn much more about the fate of the Fermi liquid (7, 32), the fact that our results approach  $L_0$  is rather surprising for a strongly correlated system without quasiparticles. In principle, the Lorenz number  $L$  can be arbitrary in the absence of long-lived quasiparticles, since neither Boltzmann theory nor the Wiedemann-Franz law should be generally applicable. However, both charge and heat transport are controlled primarily by the electronic kinetic energy at low temperatures, independent of  $U$  or  $t'$  (see Fig. S5 in the Supplementary Materials). Even though the system has no long-lived coherent quasiparticles, as indicated by the temperature dependence of  $D^{-1}$  in Fig. 2, electrical and thermal transport in this doped strongly correlated Mott insulator still appear to obey the Wiedemann-Franz law. Our results are quite generic to strongly correlated systems and provide a “beyond-Boltzmann” understanding of traditional transport ratios.

## References

1. O. Gunnarsson, M. Calandra, J. E. Han, *Rev. Mod. Phys.* **75**, 1085 (2003).
2. N. Hussey, K. Takenaka, H. Takagi, *Philos. Mag.* **84**, 2847 (2004).
3. J. M. Harris, *et al.*, *Phys. Rev. Lett.* **75**, 1391 (1995).
4. J. Ayres, *et al.*, *Nature* **595**, 661 (2021).
5. T. Kimura, *et al.*, *Phys. Rev. B* **53**, 8733 (1996).
6. C. Proust, K. Behnia, R. Bel, D. Maude, S. I. Vedenev, *Phys. Rev. B* **72**, 214511 (2005).
7. V. C. Stangier, E. Berg, J. Schmalian, *Phys. Rev. B* **105**, 115113 (2022).

8. B. Michon, *et al.*, *Phys. Rev. X* **8**, 041010 (2018).
9. R. W. Hill, C. Proust, L. Taillefer, P. Fournier, R. L. Greene, *Nature* **414**, 711 (2001).
10. X. F. Sun, *et al.*, *Phys. Rev. B* **80**, 104510 (2009).
11. C. Proust, E. Boaknin, R. W. Hill, L. Taillefer, A. P. Mackenzie, *Phys. Rev. Lett.* **89**, 147003 (2002).
12. G. Grissonnanche, *et al.*, *Phys. Rev. B* **93**, 064513 (2016).
13. S. Nakamae, *et al.*, *Phys. Rev. B* **68**, 100502 (2003).
14. J. Zhang, *et al.*, *Proceedings of the National Academy of Sciences* **114**, 5378 (2017).
15. G. Grissonnanche, *et al.*, *Nature* **571**, 376 (2019).
16. S. A. Hartnoll, *Nature Physics* **11**, 54 (2015).
17. S. A. Hartnoll, A. P. Mackenzie, *arXiv preprint arXiv:2107.07802* (2021).
18. R. Mahajan, M. Barkeshli, S. A. Hartnoll, *Phys. Rev. B* **88**, 125107 (2013).
19. T. Hartman, S. A. Hartnoll, R. Mahajan, *Phys. Rev. Lett.* **119**, 141601 (2017).
20. M. Qin, T. Schäfer, S. Andergassen, P. Corboz, E. Gull, *Annual Review of Condensed Matter Physics* **13**, 275 (2022).
21. D. P. Arovas, E. Berg, S. A. Kivelson, S. Raghu, *Annual Review of Condensed Matter Physics* **13**, 239 (2022).
22. E. W. Huang, R. Sheppard, B. Moritz, T. P. Devereaux, *Science* **366**, 987 (2019).
23. P. T. Brown, *et al.*, *Science* **363**, 379 (2019).

24. M. A. Nichols, *et al.*, *Science* **363**, 383 (2019).
25. W. Xu, W. McGehee, W. Morong, B. DeMarco, *Nature communications* **10**, 1 (2019).
26. R. Blankenbecler, D. J. Scalapino, R. L. Sugar, *Phys. Rev. D* **24**, 2278 (1981).
27. S. R. White, *et al.*, *Phys. Rev. B* **40**, 506 (1989).
28. M. Jarrell, J. E. Gubernatis, *Physics Reports* **269**, 133 (1996).
29. O. Gunnarsson, M. W. Haverkort, G. Sangiovanni, *Phys. Rev. B* **82**, 165125 (2010).
30. W. O. Wang, J. K. Ding, B. Moritz, E. W. Huang, T. P. Devereaux, *Phys. Rev. B* **105**, L161103 (2022).
31. C. H. Mousatov, I. Esterlis, S. A. Hartnoll, *Phys. Rev. Lett.* **122**, 186601 (2019).
32. E. Berg, *Private communication* .
33. D. Bergeron, A.-M. S. Tremblay, *Phys. Rev. E* **94**, 023303 (2016).
34. W. O. Wang, *et al.*, *Phys. Rev. Research* **3**, 033033 (2021).
35. R. M. Fye, *Phys. Rev. B* **33**, 6271 (1986).

## Acknowledgments

We acknowledge helpful discussions with A. Auerbach, N. E. Hussey, S. Kivelson, R. T. Scalettar, and Z. X. Shen. This work was supported by the U.S. Department of Energy (DOE), Office of Basic Energy Sciences, Division of Materials Sciences and Engineering. EWH was supported by the Gordon and Betty Moore Foundation EPiQS Initiative through the grants GBMF 4305 and GBMF 8691. YS was supported by the Gordon and Betty Moore Foundation's EPiQS



Initiative through grants GBMF 4302 and GBMF 8686. Computational work was performed on the Sherlock cluster at Stanford University and on resources of the National Energy Research Scientific Computing Center, supported by the U.S. DOE, Office of Science, under Contract no. DE-AC02-05CH11231. The data and analysis routines (Jupyter/Python) needed to reproduce the figures can be found at <https://doi.org/10.5281/zenodo.6893128>.

## **Supplementary Materials**

Methods

Supplementary Text

Figs. S1 to S10

References (33-35)

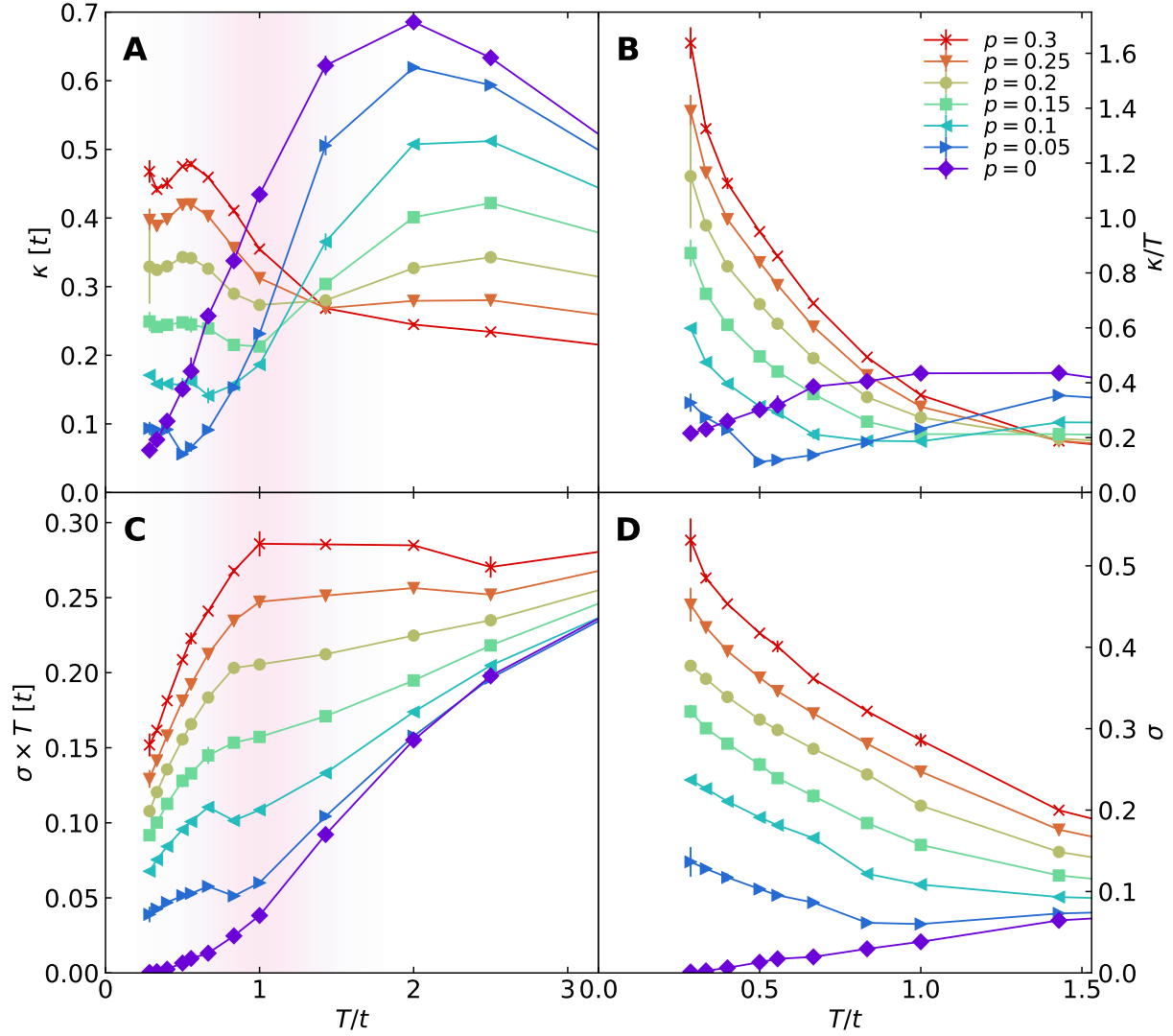


Figure 1: **Temperature and doping dependence of thermal and charge conductivity.** (A) DC thermal conductivity  $\kappa$ . (B)  $\kappa/T$  focused on the low-temperature regime. (C) DC charge conductivity  $\sigma$  multiplied by temperature  $T$ . (D)  $\sigma$  focused on the low-temperature regime. The pink-shaded area marks a rough cross-over temperature  $T_{x0}$  for both  $\kappa$  and  $\sigma \times T$ . Parameters:  $U/t = 8$  and  $t'/t = -0.25$ .

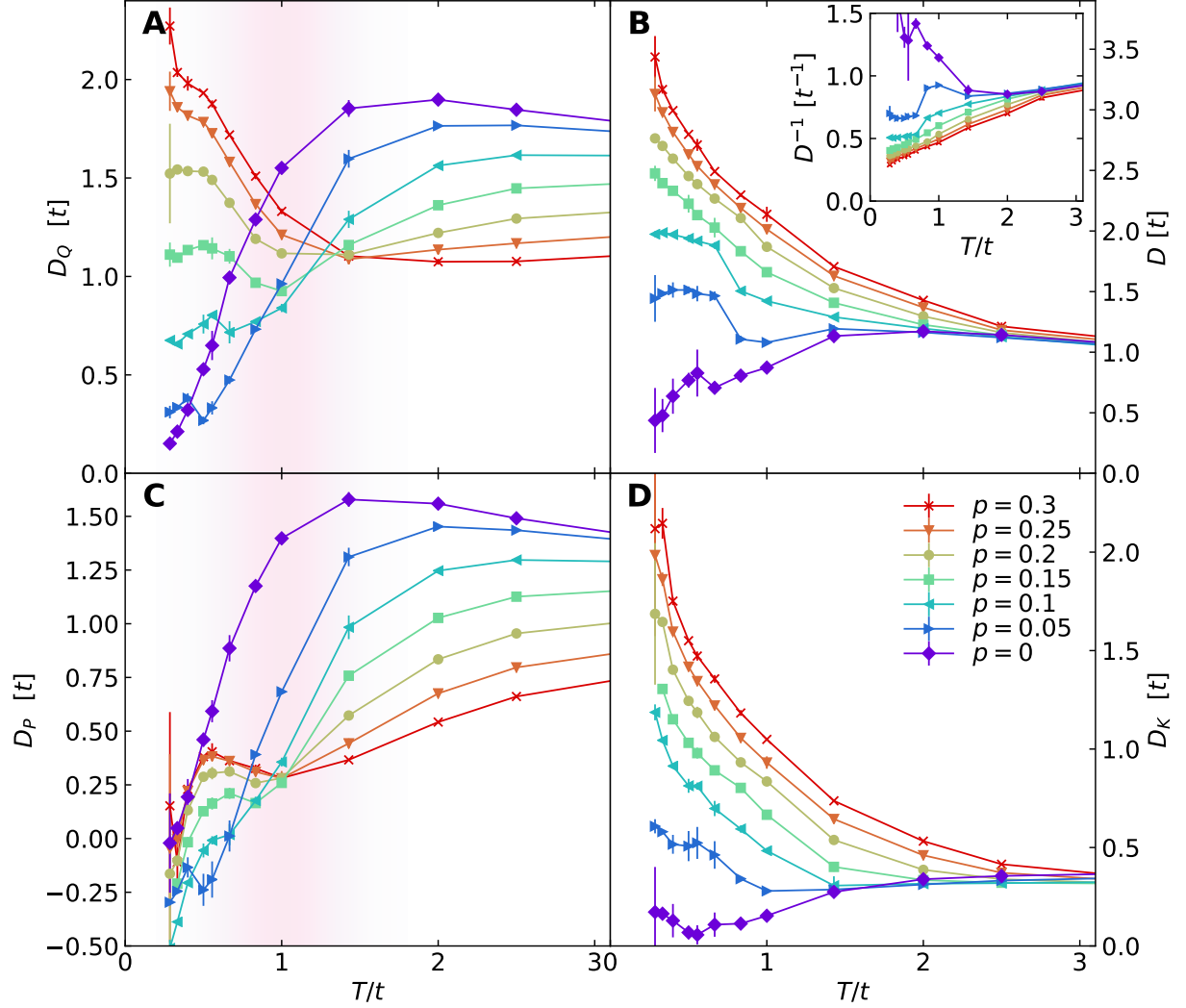


Figure 2: **Thermal diffusivity and its decomposition.** (A) Thermal diffusivity  $D_Q$ . (B) Charge diffusivity  $D$ . The inset shows the inverse charge diffusivity  $D^{-1}$ . (C) and (D) show the decomposition of thermal diffusivity  $D_Q$  into potential  $D_P$  and kinetic  $D_K$  contributions, respectively. The pink-shaded area marks a rough position for  $T_{x0}$ . Parameters:  $U/t = 8$  and  $t'/t = -0.25$ .

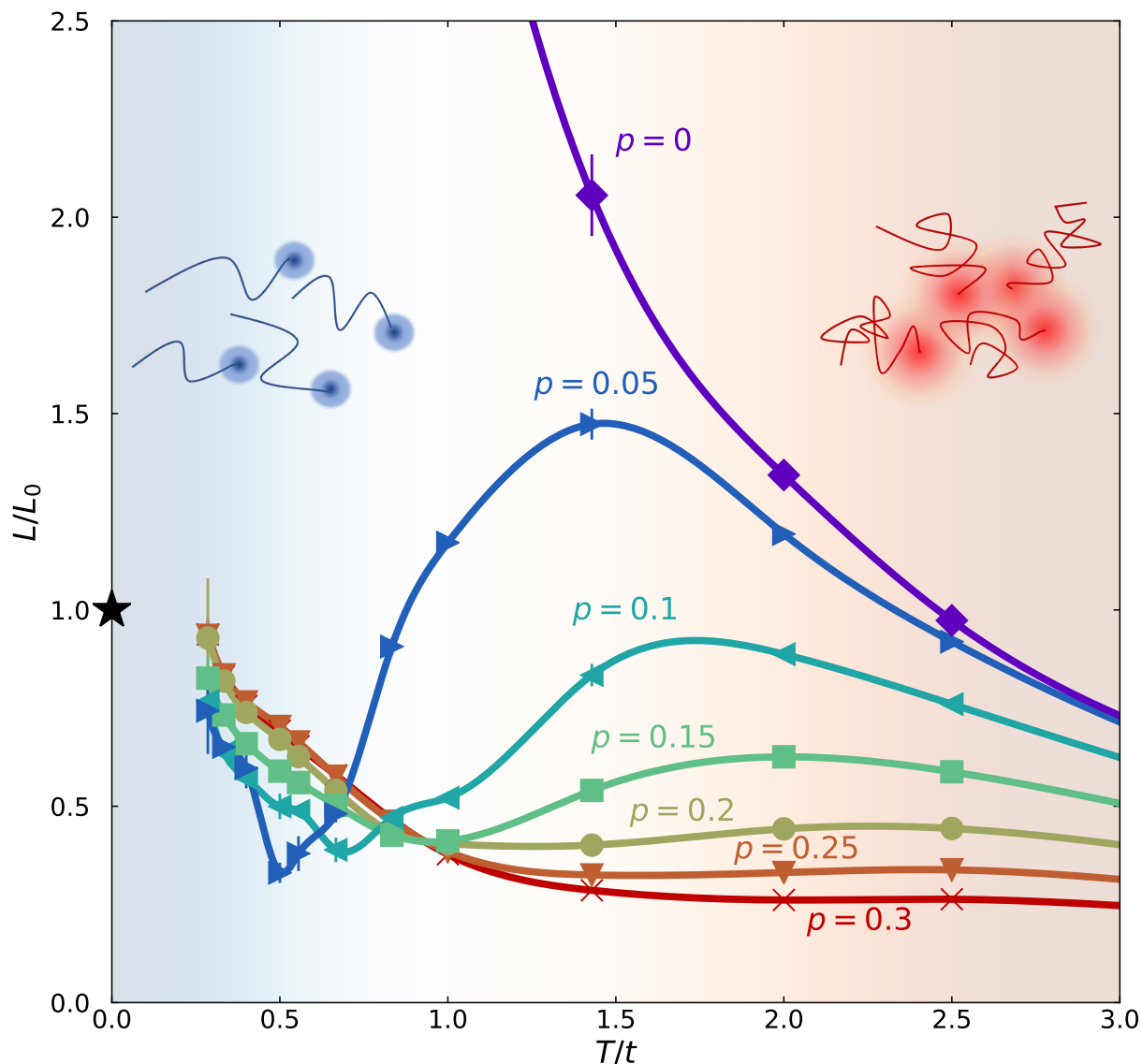


Figure 3: **Lorenz number.**  $L = \kappa/(T\sigma)$  normalized by  $L_0$ . The lines are guides to the eye. At low temperatures, below  $T_{x0}$ ,  $L/L_0$  approaches 1, marked by the black star. Parameters:  $U/t = 8$  and  $t'/t = -0.25$ . (Cartoons) At high temperatures, transport is incoherent; electrons are strongly correlated and have an extraordinarily short mean-free-path. At low temperatures, the electrons are on their way toward some sort of “coherence”; electrons have a longer mean-free-path, although not long enough for well-defined long-lived quasiparticles. While single-particle and individual transport properties show signatures of anomalous strange metal and non-Fermi liquid behavior, ratios like the Lorenz number seem to fall in line with the Fermi liquid paradigm.

# Supplementary Materials

## Methods

### Simulation Parameters

Simulations of the 2D single-band  $t$ - $t'$ - $U$  Hubbard model were performed on  $8 \times 8$  square lattice clusters with periodic boundary conditions for next-nearest-neighbour hopping  $t' = -0.25t$  and on-site Coulomb repulsion  $U = 8t$ . Measurements of all quantities, other than the density in the  $\mu$  tuning process described later, if not otherwise specified, were performed with a maximum imaginary time Trotter discretization  $d\tau = 0.05/t$ , within the determinant quantum Monte Carlo (DQMC) algorithm (26, 27). At high temperatures, the smallest number of imaginary-time slices used in the Trotter decomposition was  $\tilde{L} = \beta/d\tau = 20$ , where  $\beta$  is the inverse temperature  $T^{-1}$ . Each Markov chain in the Monte Carlo process consisted of  $5 \times 10^4$  warm up sweeps and  $10^6$  measurement sweeps through space-time. Unequal time measurements were taken every 4 sweeps. Measurements were made on up to  $\sim 2400$  Markov chains for each set of parameters at the lowest temperatures, with  $2.5 \times 10^5$  unequal time measurements and  $2 \times 10^5 \times \tilde{L}$  equal time measurements [or  $2.5 \times 10^5 \times \tilde{L}$  equal time measurements, if  $\text{mod}(\tilde{L}, 5) \neq 0$ ] per chain.

### Analytic Continuation

We evaluated DC transport coefficients using the Kubo formula (30) to determine  $\kappa$  and  $\sigma$ . The transport coefficients were obtained from DQMC simulation measurements of the corresponding correlation functions in imaginary time. The maximum entropy analytic continuation (MaxEnt) (28, 29, 33) algorithm was used to obtain DC values. Details of the formalism, operators, and specific correlation functions can be found in the “Formalism” section of the Supplementary Text.

The MaxEnt algorithm requires a “model” function to regularize the real-frequency correla-

tion function. Here, we used an annealing procedure where spectra from one temperature serve as the model function for the next lower temperature in a sequence (22, 30). We also determined spectra in the infinite-temperature-limit, using the moments expansion method (22, 30) (up to sixth order, or eighth order for  $t' = 0$ ), which served as the model function at the highest temperature.

### Chemical Potential Tuning

To tune the chemical potential  $\mu$  for a specific target filling  $n_{\text{tar}} = 1 - p_{\text{tar}}$  at a given temperature and lattice size, we used DQMC to calculate  $\langle n \rangle$  over a range of chemical potentials  $\mu$  (at  $0.05t$  intervals). We obtained the best  $\mu$  by interpolation of  $\langle n \rangle$  versus  $\mu$ . For the tuning process, the imaginary time discretization  $d\tau$  was chosen to be  $0.02/t$ . The doping  $p$  in each figure indicates the target doping  $p_{\text{tar}}$ .

### Error Analysis

Error bars are shown for all measurements. If not otherwise specified, error bars are determined by bootstrap resampling. We calculated 100 bootstraps and used the standard deviation of the distribution as the standard error of the mean. The mean values represent the average values from bootstrap resampling. For analytic continuation, the average spectra from bootstrap resampling at one temperature served as a model function for the next lower temperature, as described above for annealing.

## **Supplementary Text**

### Formalism

In this paper,  $\kappa$  always refers to the longitudinal DC thermal conductivity measured under the condition of zero charge current (30), distinguished from the one measured under the condition of zero electric field;  $c_v$  refers to the specific heat, defined as the energy density difference of the system per temperature difference at fixed density. Charge  $e$ ,  $k_B$ , and  $\hbar$  are set to 1

throughout the paper.

We investigate the 2D single-band Hubbard model with spin  $S = 1/2$ . Considering both nearest-neighbour and the next-nearest-neighbour hopping, the Hamiltonian is

$$\begin{aligned}
H = & -t \sum_{\langle lm \rangle \sigma} (c_{l\sigma}^\dagger c_{m\sigma} + c_{m\sigma}^\dagger c_{l\sigma}) - t' \sum_{\langle\langle lm \rangle\rangle \sigma} (c_{l\sigma}^\dagger c_{m\sigma} + c_{m\sigma}^\dagger c_{l\sigma}) \\
& + U \sum_l (n_{l\uparrow} - \frac{1}{2})(n_{l\downarrow} - \frac{1}{2}), \tag{1}
\end{aligned}$$

where  $t$  ( $t'$ ) is the nearest-neighbour (next-nearest-neighbour) hopping,  $U$  is the on-site Coulomb interaction,  $c_{l,\sigma}^\dagger$  ( $c_{l,\sigma}$ ) is the creation (annihilation) operator for an electron at site  $l$  with spin  $\sigma$ , and  $n_{l,\sigma} \equiv c_{l,\sigma}^\dagger c_{l,\sigma}$  is the number operator at site  $l$ .

Expressions for  $c_v$ ,  $\kappa$  and  $\sigma$  have been derived in the Supplementary Materials in Ref. (30). As in Ref. (30), there are two methods to calculate  $c_v$ . One is to measure the average energy  $\langle H \rangle$  at different temperatures for fixed densities, and directly calculate  $\delta(\langle H \rangle / V) / \delta T$  by choosing a reasonable finite temperature interval  $\delta T$  – the finite difference method. The other method is to use the expression

$$c_v = \frac{\beta}{V} (\Lambda_{HH} - \frac{\Lambda_{HN}^2}{\Lambda_{NN}}), \tag{2}$$

referred to below as the fluctuation method. Here,  $\Lambda_{O_1 O_2} = \beta(\langle O_1 O_2 \rangle - \langle O_1 \rangle \langle O_2 \rangle)$ , where  $N$  is the operator for the total number of particles in the system,  $\beta = 1/T$  is the inverse temperature, and  $V$  is the volume. Similarly, the charge compressibility can be calculated using the fluctuation method  $\chi = \Lambda_{NN} / V$ . The fluctuation method is used for calculating both  $c_v$  and  $\chi$  when determining both  $D_Q$  and  $D$ , respectively. Figure S1 shows the DQMC results for **(A)** the specific heat  $c_v$  and **(B)** the charge compressibility  $\chi$  (22). Note that in Fig. S1**(A)** the results for  $c_v$  are consistent between the finite difference and fluctuation methods.

Calculating  $\sigma$  and  $\kappa$  requires correlation functions that include the particle/charge current  $\mathbf{J}$  and energy current  $\mathbf{J}_E$  terms. From the Hamiltonian in Eq. 1, we derive  $\mathbf{J}$  and  $\mathbf{J}_E$  in a manner

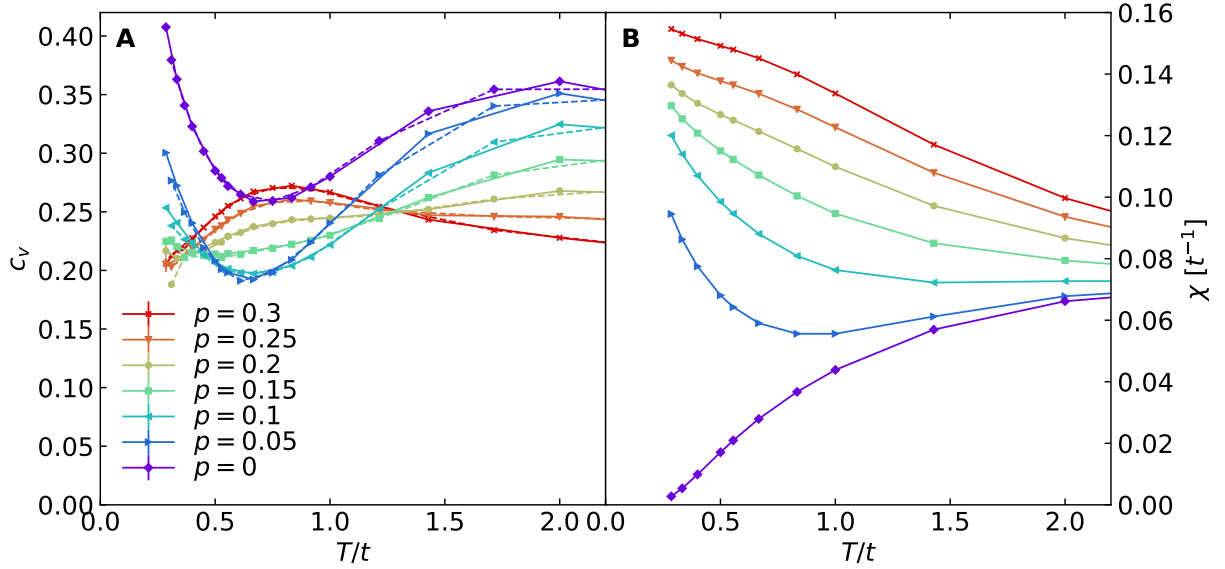


Figure S1: **(A)** Specific heat  $c_v$ . Solid lines are results from the fluctuation method and dashed lines are the results from the finite difference method. **(B)** Charge compressibility  $\chi$ . Error bars for  $c_v$  and  $\chi$  are  $\pm 1$  standard error determined by jackknife resampling. Proper error propagation is used for  $c_v$  obtained from the finite difference method. Simulation parameters are the same as the main text.

similar to that in Ref. (30),

$$\begin{aligned}
 \mathbf{J} &= \frac{t}{2} \sum_{l, \delta \in \{\delta\}, \sigma} \delta (i c_{l+\delta, \sigma}^\dagger c_{l, \sigma} + h.c.) \\
 &+ \frac{t'}{2} \sum_{l, \delta' \in \{\delta'\}, \sigma} \delta' (i c_{l+\delta', \sigma}^\dagger c_{l, \sigma} + h.c.)
 \end{aligned} \tag{3}$$



and

$$\begin{aligned}
\mathbf{J}_E = & \sum_{l, \delta_1 \in \{\delta\}, \delta_2 \in \{\delta\}, \sigma} \left(-\frac{\delta_1 + \delta_2}{4}\right) t^2 (i c_{l+\delta_1+\delta_2, \sigma}^\dagger c_{l, \sigma} + h.c.) \\
& + \sum_{l, \delta \in \{\delta\}, \delta' \in \{\delta'\}, \sigma} \left(-\frac{\delta + \delta'}{2}\right) t t' (i c_{l+\delta+\delta', \sigma}^\dagger c_{l, \sigma} + h.c.) \\
& + \sum_{l, \delta'_1 \in \{\delta'\}, \delta'_2 \in \{\delta'\}, \sigma} \left(-\frac{\delta'_1 + \delta'_2}{4}\right) t'^2 (i c_{l+\delta'_1+\delta'_2, \sigma}^\dagger c_{l, \sigma} + h.c.) \\
& + \frac{Ut}{4} \sum_{l, \delta \in \{\delta\}, \sigma} \delta (n_{l+\delta, \bar{\sigma}} + n_{l, \bar{\sigma}}) (i c_{l+\delta, \sigma}^\dagger c_{l, \sigma} + h.c.) \\
& + \frac{Ut'}{4} \sum_{l, \delta' \in \{\delta'\}, \sigma} \delta' (n_{l+\delta', \bar{\sigma}} + n_{l, \bar{\sigma}}) (i c_{l+\delta', \sigma}^\dagger c_{l, \sigma} + h.c.) \\
& \quad - \frac{Ut}{4} \sum_{l, \delta \in \{\delta\}, \sigma} \delta (i c_{l+\delta, \sigma}^\dagger c_{l, \sigma} + h.c.) \\
& \quad - \frac{Ut'}{4} \sum_{l, \delta' \in \{\delta'\}, \sigma} \delta' (i c_{l+\delta', \sigma}^\dagger c_{l, \sigma} + h.c.), \tag{4}
\end{aligned}$$

where  $\{\delta\}$  ( $\{\delta'\}$ ) includes all position displacements for nearest neighbours (next-nearest neighbours). Specifically, on a 2D square lattice we consider  $\{\delta\} = \{+\mathbf{x}, -\mathbf{x}, +\mathbf{y}, -\mathbf{y}\}$  and  $\{\delta'\} = \{+\mathbf{x} + \mathbf{y}, -\mathbf{x} + \mathbf{y}, +\mathbf{x} - \mathbf{y}, -\mathbf{x} - \mathbf{y}\}$ , where the lattice constant is set to 1 and  $\mathbf{x}$  and  $\mathbf{y}$  are unit vectors. Here, the spin index satisfies  $\bar{\sigma} = -\sigma$ . The first three lines of Eq. 4 define the kinetic energy current  $\mathbf{J}_K$ , and the fourth and fifth lines correspond to the four-fermion potential energy current  $\mathbf{J}_P$ . The last two lines of Eq. 4 are corrections proportional to  $\mathbf{J}$ , originating from the chemical-potential correction term  $-\frac{1}{2}UN$  in the Hamiltonian of Eq. 1.

Fourier transforming the fermion operators such as

$$c_{l, \sigma}^\dagger = \frac{1}{\sqrt{V}} \sum_{\mathbf{k}} e^{-i\mathbf{k} \cdot \mathbf{R}_l} c_{\mathbf{k}, \sigma}^\dagger, \tag{5}$$

we can transform Eq. 3, and the first three lines of Eq. 4 ( $\mathbf{J}_K$ ), which yields

$$\mathbf{J} = \sum_{\mathbf{k}, \sigma} \mathbf{v}_{\mathbf{k}} c_{\mathbf{k}, \sigma}^\dagger c_{\mathbf{k}, \sigma}, \tag{6}$$

$$\mathbf{J}_K = \sum_{\mathbf{k}, \sigma} \epsilon_{\mathbf{k}} \mathbf{v}_{\mathbf{k}} c_{\mathbf{k}, \sigma}^\dagger c_{\mathbf{k}, \sigma}, \tag{7}$$

as summations in  $\mathbf{k}$ -space. Here,  $\epsilon_{\mathbf{k}}$  is the band energy at momentum  $\mathbf{k}$ , determined by the  $U = 0$  non-interacting limit of the Hamiltonian in Eq. 1,  $H(U = 0) = \sum_{\mathbf{k},\sigma} \epsilon_{\mathbf{k}} c_{\mathbf{k},\sigma}^\dagger c_{\mathbf{k},\sigma}$ , and the band velocity  $\mathbf{v}_{\mathbf{k}} \equiv \partial\epsilon_{\mathbf{k}}/\partial\mathbf{k}$ .

As mentioned in the main text, we can understand  $\mathbf{J}_P$  as the flow of double occupancies, by looking at its operator form compared to the charge current  $\mathbf{J}$ . As a summation over real space, each term in  $\mathbf{J}_P$  is similar to that in  $\mathbf{J}$ , involving electrons with spin  $\sigma$  flowing between sites. In  $\mathbf{J}_P$  this includes a prefactor of density operators with opposite spin; and  $\mathbf{J}_P$  selects charge flow involving a process where an electron flows from/to a site already occupied by an electron of opposite spin. In other words, nonzero contributions to  $\mathbf{J}_P$  rely on breaking and reforming double occupancies.

Using the Kubo formula, the transport coefficient are defined as (30)

$$L_{O_1 O_2}(\omega) = \frac{1}{V\beta} \int_0^\infty d\tilde{t} e^{i(\omega+i0^+)\tilde{t}} \int_0^\beta d\tau \langle O_1(\tilde{t} - i\tau) O_2(0) \rangle, \quad (8)$$

where  $O_1$  and  $O_2$  are Hermitian operators that can be chosen as any one of the current operators introduced previously.  $\tilde{t}$  is real time and

$$O_1(\tilde{t} - i\tau) = e^{i(H-\mu N)(\tilde{t}-i\tau)} O_1 e^{-i(H-\mu N)(\tilde{t}-i\tau)}. \quad (9)$$

We consider  $O_1 = O_2 = O$ , and set  $Z = \text{Tr}(e^{-\beta(H-\mu N)})$  as the partition function. From Eq. 8, we obtain

$$\begin{aligned} \text{Re } L_{OO}(\omega) &= \frac{\pi}{ZV\beta\omega} \sum_{i_1, i_2} \|\langle i_1 | O | i_2 \rangle\|^2 \\ &\quad \times e^{-\beta E_{i_1}} (1 - e^{-\beta\omega}) \delta(\omega + E_{i_1} - E_{i_2}), \end{aligned} \quad (10)$$

where  $|i_i\rangle$  ( $E_{i_i}$ ) are eigenstates (eigenvalues) of  $H - \mu N$ . We use DQMC to measure the correlation functions in imaginary time

$$\begin{aligned} \langle T_\tau O(\tau) O(0) \rangle &\equiv \frac{1}{Z} \text{Tr}(e^{-\beta(H-\mu N)} T_\tau e^{\tau(H-\mu N)} O e^{-\tau(H-\mu N)} O) \\ &= \frac{1}{Z} \sum_{i_1, i_2} \|\langle i_1 | O | i_2 \rangle\|^2 e^{-\beta E_{i_1}} e^{\tau(E_{i_1} - E_{i_2})}. \end{aligned} \quad (11)$$

We then apply MaxEnt (28, 29) to  $\langle T_\tau O(\tau)O(0) \rangle$  and obtain  $\text{Re } L_{OO}(\omega)$  (22, 30) using the relation (34)

$$\frac{1}{V\beta} \langle T_\tau O(\tau)O(0) \rangle = \int_0^\infty d\omega \text{Re } L_{OO}(\omega) \frac{\omega \cosh[\omega(\tau - \beta/2)]}{\pi \sinh[\beta\omega/2]}, \quad (12)$$

which can be derived from Eqs. 10 and 11.  $L_{OO}(\omega)$  is guaranteed to be positive definite in Eq. 8 when  $O_1 = O_2 = O$ .

In this work, particle-hole symmetry is broken and chemical potential  $\mu$  is not 0; thus, to measure thermal conductivity  $\kappa$  and the kinetic-potential decomposition  $\kappa_K$  and  $\kappa_P$ , we need to analytically continue more correlation functions in addition to those in Ref. (30). Here, we measure  $\langle T_\tau O(\tau)O(0) \rangle$  and apply MaxEnt for  $O \in \{J_x, J_{Q,x}, J_{K,x}, J_{P',x}, J_{Q,x} + J_x, J_{K,x} + J_x, J_{P',x} + J_x\}$ . Here, “ $x$ ” is the  $x$  direction and  $J_{P',x}$  is defined as  $J_{P,x} - (U/2 + \mu)J_x$ . For convenience, we define  $L[O] = L_{OO}$ , which we obtain directly from analytic continuation.

We previously derived the kinetic/potential contribution to the longitudinal thermal conductivity under the condition of zero electrical current as (30)

$$\kappa_{K/P} = \beta^2 \left( L_{J_{K/P,x}J_{Q,x}} - \frac{L_{J_{K/P,x}J_x} L_{J_x J_{Q,x}}}{L_{J_x J_x}} \right), \quad (13)$$

where  $L_{O_1 O_2}$  is defined in Eq. 8. Here, we transform Eq. 13 to

$$\kappa_P = \beta^2 \left( L_{J_{P',x}J_{Q,x}} - \frac{L_{J_{P',x}J_x} L_{J_x J_{Q,x}}}{L_{J_x J_x}} \right), \quad (14)$$

As discussed below, even though the expressions are equivalent, using  $J_{P',x}$  instead of  $J_{P,x}$  in the relevant transport coefficients is a strategy to reduce error propagation. There can be multiple ways to choose correlations for analytic continuation and combine them to calculate Eq. 13 or Eq. 14. Different choices can result in different magnitudes for the final statistical error after error propagation. We know that subtracting large measurements and producing a small result can lead to large statistical errors relative to the difference. Generally speaking, to reduce the statistical error of a result from an expression like Eq. 13 or Eq. 14, we want to

minimize the relative error of both terms before subtraction, and we also want to minimize the magnitudes of the two terms. Here, our choice is as follows:  $\kappa$  is calculated using

$$\kappa = \beta^2 \left( L[J_{Q,x}] - \frac{L_{J_{Q,x}J_x}^2}{L[J_x]} \right), \quad (15)$$

where  $L_{J_{Q,x}J_x}$  is calculated from  $L_{J_{Q,x}J_x} = (L[J_{Q,x} + J_x] - L[J_{Q,x}] - L[J_x])/2$ . We define and calculate  $\kappa_{K,0}$  and  $\kappa_{P',0}$  as

$$\begin{aligned} \kappa_{K,0} &= \beta^2 \left( L[J_{K,x}] - \frac{L_{J_{K,x}J_x}^2}{L[J_x]} \right), \\ \kappa_{P',0} &= \beta^2 \left( L[J_{P',x}] - \frac{L_{J_{P',x}J_x}^2}{L[J_x]} \right), \end{aligned} \quad (16)$$

where  $L_{J_{K,x}J_x}$  and  $L_{J_{P',x}J_x}$  are calculated from

$$\begin{aligned} L_{J_{K,x}J_x} &= (L[J_{K,x} + J_x] - L[J_{K,x}] - L[J_x])/2, \\ L_{J_{P',x}J_x} &= (L[J_{P',x} + J_x] - L[J_{P',x}] - L[J_x])/2. \end{aligned} \quad (17)$$

Then from Eqs.13-16, we have

$$\kappa_K = \kappa_{K,0} + (\kappa - \kappa_{K,0} - \kappa_{P',0})/2, \quad (18)$$

$$\kappa_P = \kappa_{P',0} + (\kappa - \kappa_{K,0} - \kappa_{P',0})/2, \quad (19)$$

which are used for the calculation of  $\kappa_K$  and  $\kappa_P$ .

Besides  $\kappa$  in Eq. 15, which is measured under the condition of zero charge current, one may also be interested in the behaviors of DC thermal conductivity measured under the condition of zero electric field (30),

$$\kappa_o = \beta^2 L[J_{Q,x}]. \quad (20)$$

In Figs. S2(A) and (B), we show and compare the results of  $\kappa$  and  $\kappa_o$ , respectively. In Figs. S2(C) and (D), we compare the Lorenz number  $L \equiv \kappa/(T\sigma)$  and  $L_o \equiv \kappa_o/(T\sigma)$ , which uses  $\kappa$  and  $\kappa_o$  in the ratio, respectively. We find that in the temperature regime considered here,  $\kappa$  and

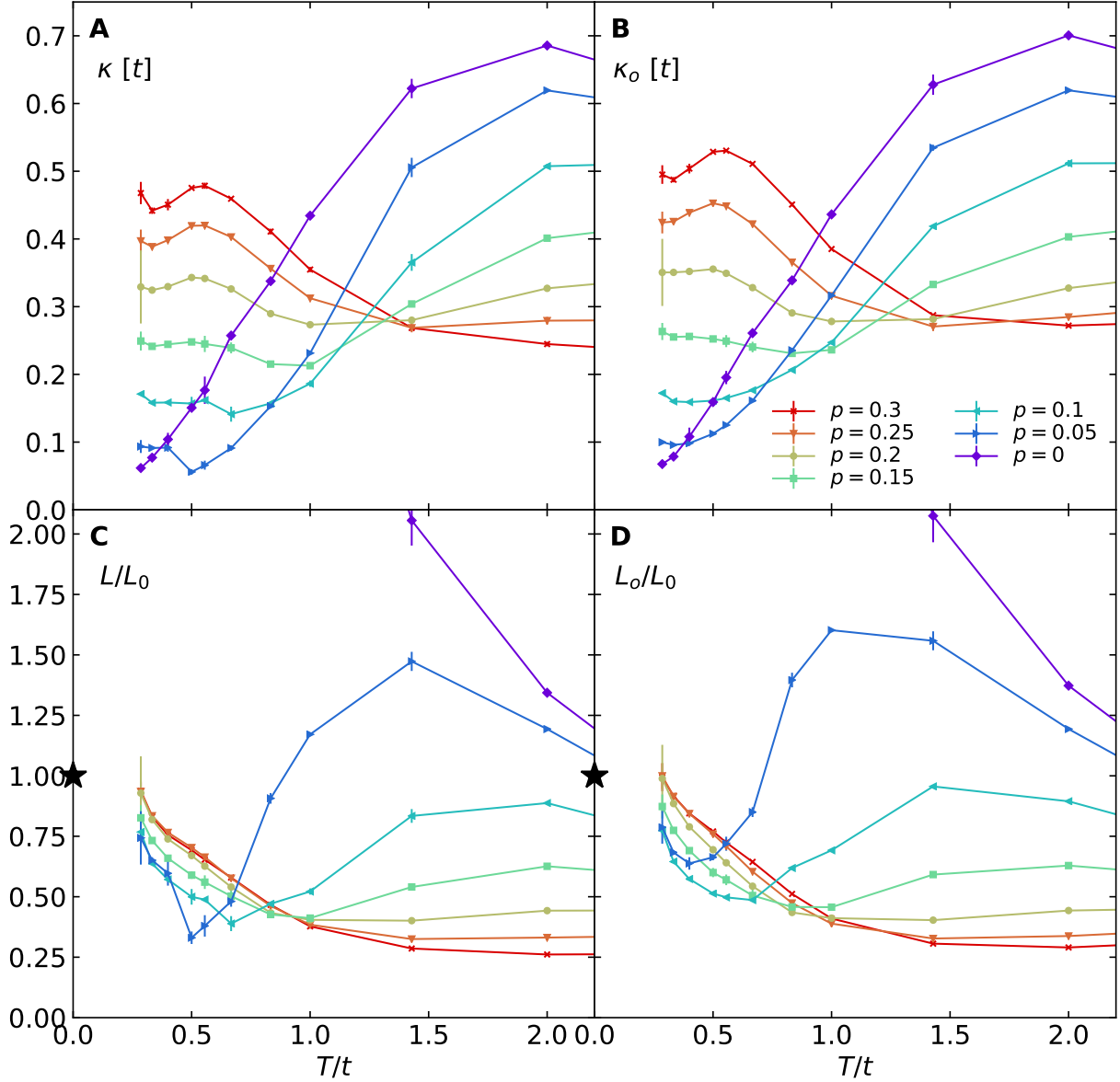


Figure S2: (A) DC thermal conductivity  $\kappa$  for zero charge current, the same as Fig. 1(A) in the main text. (B) DC thermal conductivity  $\kappa_o$  for zero electric field. (C) Lorenz number  $L \equiv \frac{\kappa}{T\sigma}$  normalized by  $L_0 \equiv \pi^2/3$ , the same as Fig. 3 in the main text. (D) Lorenz number  $L_o \equiv \frac{\kappa_o}{T\sigma}$  normalized by  $L_0$ . Simulation parameters are the same as the main text.

$\kappa_o$ , as well as  $L$  and  $L_o$ , show similar temperature and doping dependence and have similar magnitudes.

### Different Ways of Constructing Model function

Model function dependence of the results for the Lorenz number are shown in Fig. S3. Other than the annealing procedure from high to low temperature, as in the main text, we have annealed from low to high temperature by starting the procedure using results at the lowest temperature as the initial model function. Two other methods include using the model functions constructed from the infinite-temperature-limit spectra for all temperatures; and using a flat model function for all temperatures. As shown in Fig. S3, results using these different methods show qualitatively similar behavior and conclusions and discussion in the main text would remain the same regardless of the choice in model function and procedure.

### Independent Diffusivities

As mentioned in the main text,  $D_Q$  and  $D$  are not independent diffusivities due to non-zero thermoelectric effects in our model. But in this section, we will show that the corrections  $D_{\text{corr}}$  due to thermoelectric effects are neglectable compared with  $D_Q$  and  $D$ . So  $D_Q$  and  $D$  are approximately equal to independent diffusivities  $D_{\pm}$ . According to Refs. (16, 31),  $D_{\pm}$  are determined by

$$D_+ D_- = D D_Q \quad (21)$$

$$D_+ + D_- = D + D_Q + D_{\text{corr}}, \quad (22)$$

where  $D_{\text{corr}}$  is the correction term defined in Refs. (16, 31). From Fig. S4, we observe that  $D_{\text{corr}}$  is orders of magnitude smaller than either  $D_Q$  or  $D$ . Therefore, according to Eqs. 21 and 22, values of  $D_{\pm} \approx D$  and  $D_Q$ . At high temperatures,  $D_Q$  is larger than  $D$  and  $D_+ \approx D_Q$ , as can be seen in Figs. S4(A) and (D). At low temperatures where  $D$  becomes larger than  $D_Q$ ,  $D_+ \approx D$ , as can be seen in Figs. S4(B) and (D).  $D_-$  in Fig. S4(C) takes the smaller value between  $D_Q$

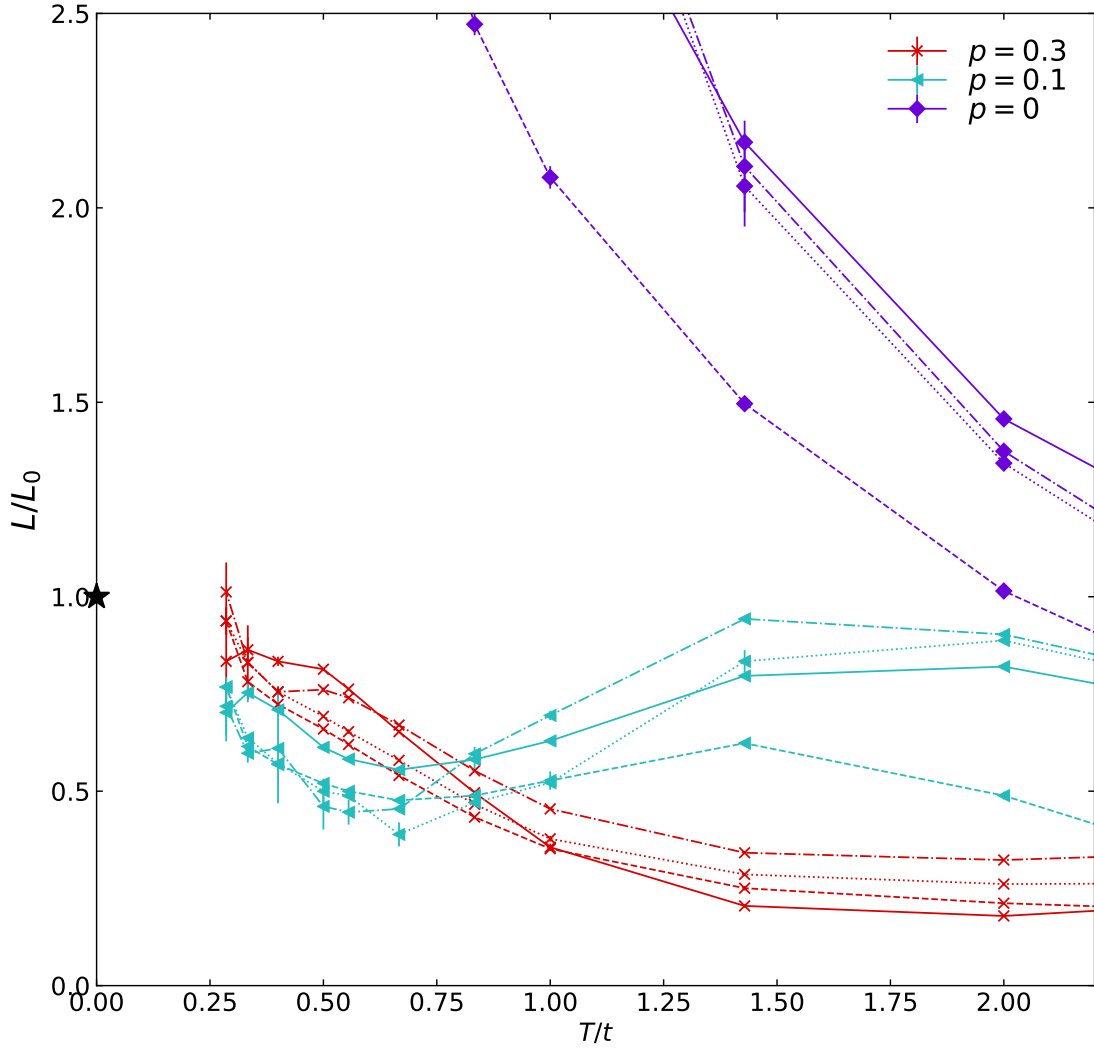


Figure S3: Lorenz number  $L$  obtained using MaxEnt with different methods for selecting the model function. Dotted lines are results from the main text, obtained using the annealing procedure from high to low temperature. Dashed lines are results using an annealing procedure from low to high temperature. Dashed dotted lines are results using the model functions constructed from the infinite-temperature-limit for all temperatures. Solid lines are results using a flat model function for all temperatures. Simulation parameters are the same as the main text.

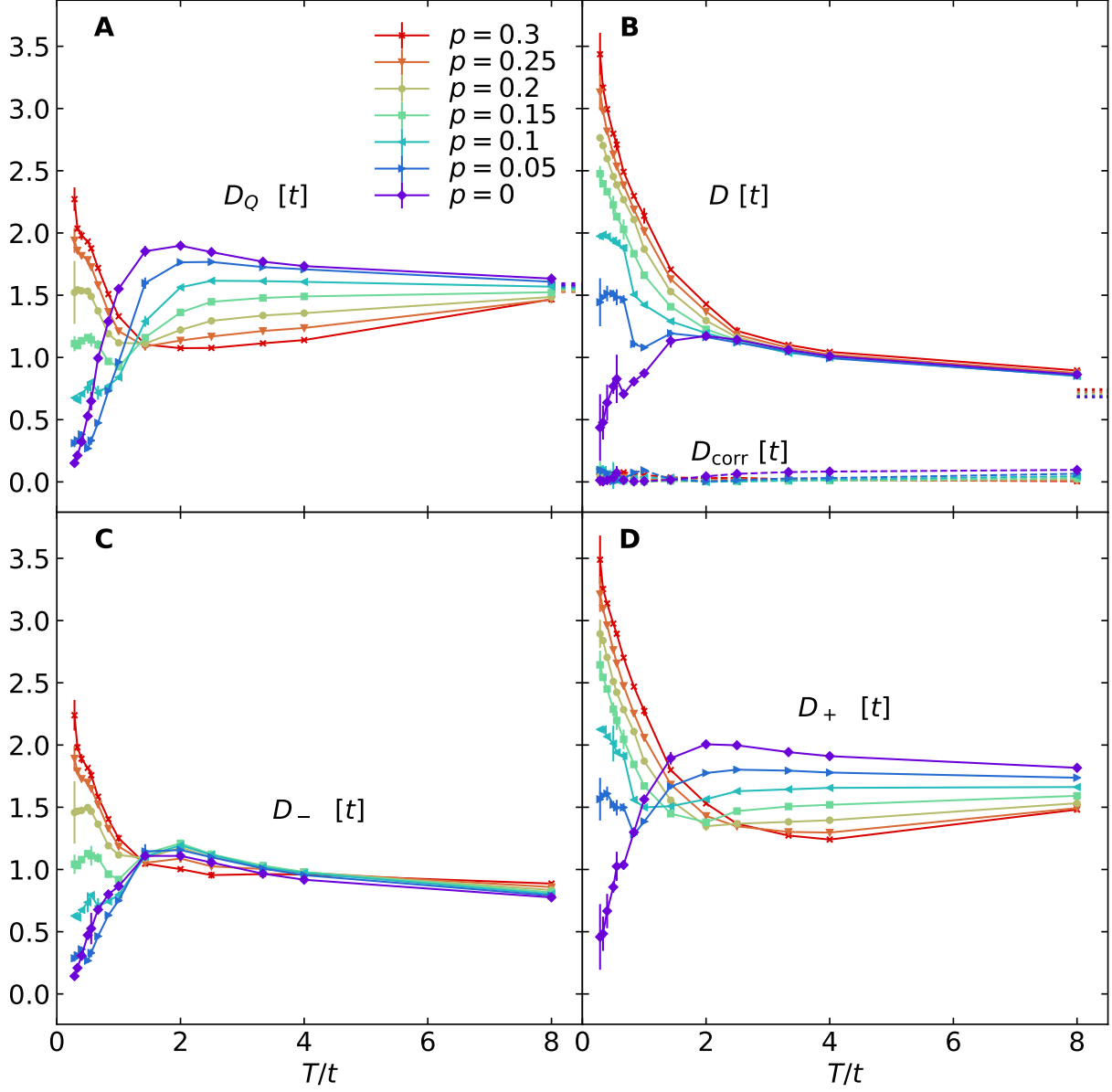


Figure S4: Comparisons between  $D_Q$ ,  $D$ ,  $D_{\text{corr}}$  and  $D_{\pm}$ . Simulation parameters are the same as the main text. (A) Thermal diffusivity  $D_Q$ . (B) Solid lines are the charge diffusivity  $D$ , and the dashed lines are the correction term  $D_{\text{corr}}$ . (C)  $D_-$ . (D)  $D_+$ . Dotted lines are infinite-temperature-limits obtained by the moments expansion method.



and  $D$ . In the high temperature limit,  $D_+$  is about twice of that of  $D_-$ , consistent with Ref. (31).

### Supplementary Data Sets

To test the generality of the conclusions in the main text, we also calculate the Lorenz number  $L$  for four other sets of parameters, as shown in Fig. S5. The lowest temperature we can achieve is lower for smaller  $U$  due to a better behaved fermion sign. The behavior of  $L$  for each parameter set is qualitatively similar, and  $L$  for each of the doped cases approaches  $L_0$  as temperature approaches zero, demonstrating that our conclusions should be quite general for the 2D correlated single-band Hubbard model.

In Fig. S6, measurements up to  $T/t = 8$  are shown and compared with corresponding infinite-temperature limits. We can see that all of the measurements approach their corresponding infinite-temperature limits as temperature increases. Transport properties in the infinite-temperature limit can be calculated using the moments expansion method. The infinite-temperature limits of  $c_v$  and  $\chi$ , given by fluctuations  $\Lambda_{O_1 O_2}$ , can be calculated analytically. Since  $e^{\beta H} = 1$ ,

$$\begin{aligned}\langle O_1 O_2 \rangle &= \text{Tr}(O_1 O_2), \\ \langle O_1 \rangle &= \text{Tr}(O_1).\end{aligned}\tag{23}$$

The calculation of these traces is straightforward in the occupation basis, when  $O_1$  and  $O_2$  are expressed in fermion operators  $c_{l,\sigma}^\dagger$  and  $c_{l,\sigma}$ .

### Trotter Error Analysis

Trotter error enters our measurements of thermodynamic and transport properties in two ways. The first is in measurements of density  $\langle n \rangle$  during chemical potential tuning. After the chemical potential  $\mu$  has been obtained for the target density, the Trotter error enters in the measurements themselves. For chemical potential tuning, Fig. S7 shows the difference between the measured density  $\langle n \rangle$  and the target density  $n_{\text{tar}}$  for different  $d\tau$ . For  $U/t = 10$  in (A)-(C), we see that the Trotter error scales as  $\sim d\tau^2$ , as predicted (35). Extrapolating

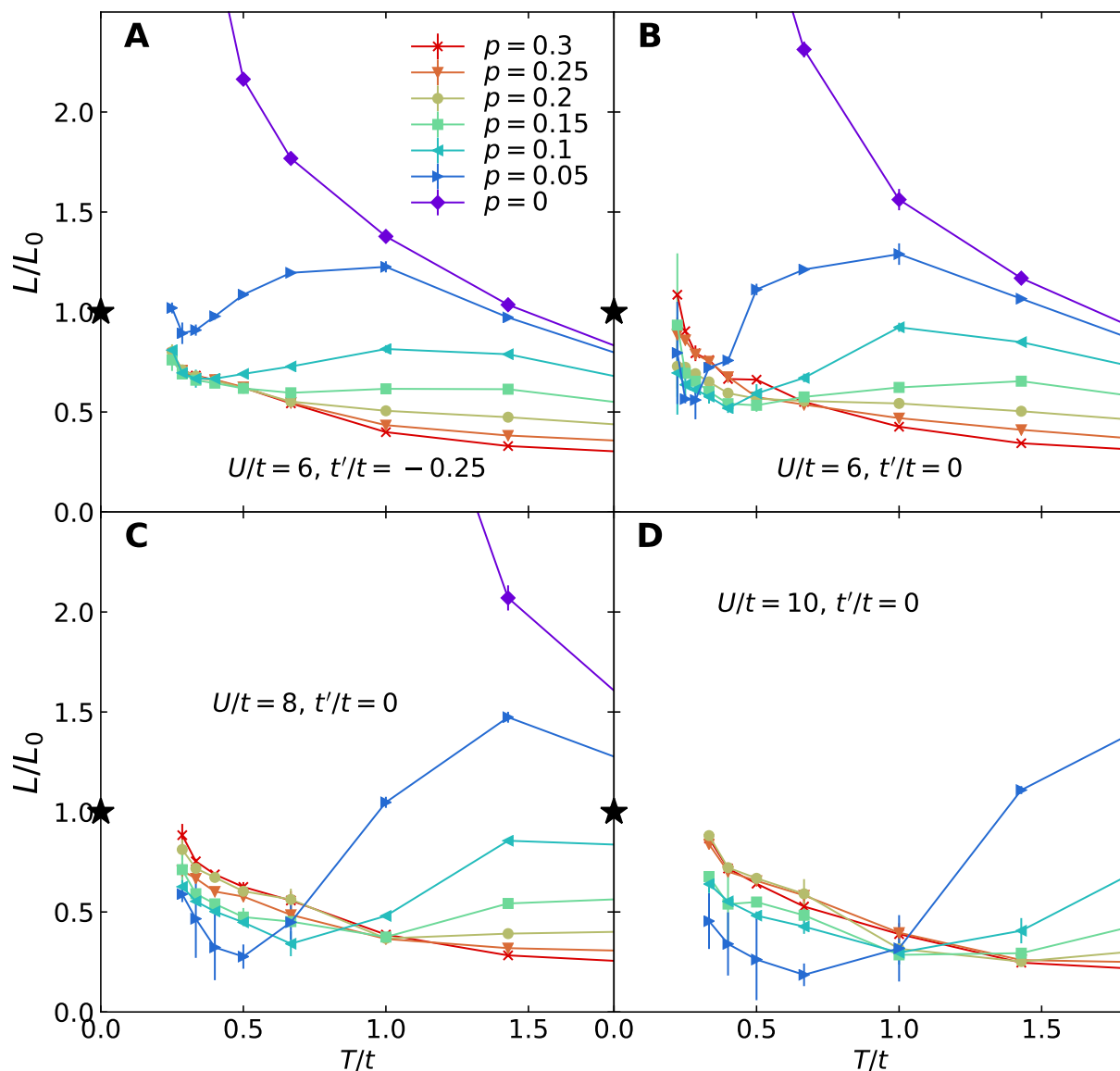


Figure S5: Supplementary data for the Lorenz number for other parameters. (A)-(D) Four sets of data with different interaction  $U$  and next-nearest-neighbour hopping  $t'$ , as indicated in each panel. Simulation cluster is  $8 \times 8$ .

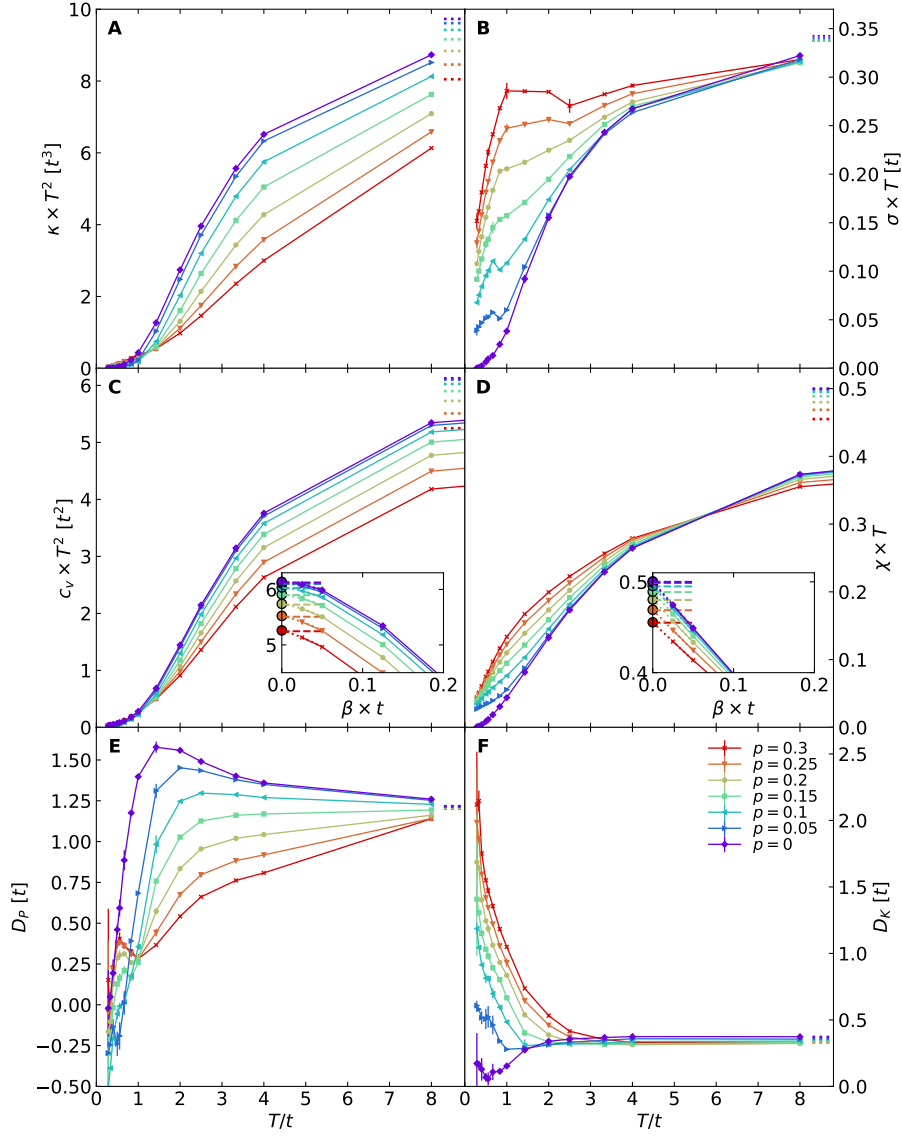


Figure S6: Behavior over a large range of temperatures for (A)  $\kappa \times T^2$ , (B)  $\sigma \times T$ , (C)  $c_v \times T^2$ , (D)  $\chi \times T$ , (E)  $D_P$ , and (F)  $D_K$ , and a comparison to infinite temperature limits for each quantity. The high-temperature dotted lines in (A) and (B) are infinite-temperature limits calculated from the moments expansion method. The high-temperature dotted lines in (C) and (D) are infinite-temperature limits calculated analytically.  $c_v$  is calculated using the fluctuation method. Insets for (C) and (D) are  $c_v \times T^2$  and  $\chi \times T$  versus  $\beta \times t$ , respectively, including data for temperatures  $T/t \geq 8$ . In these insets, the dashed lines again mark the infinite-temperature limits; and the filled circles mark cubic spline extrapolated positions for  $\beta t = 0$ . (The interpolation function is indicated by the dotted lines.) The high-temperature dotted lines in (E) and (F) are infinite-temperature limits calculated by combining transport coefficients from the moments expansion and thermodynamic properties ( $c_v$  and  $\chi$ ) calculated analytically. Simulation parameters are the same as the main text.

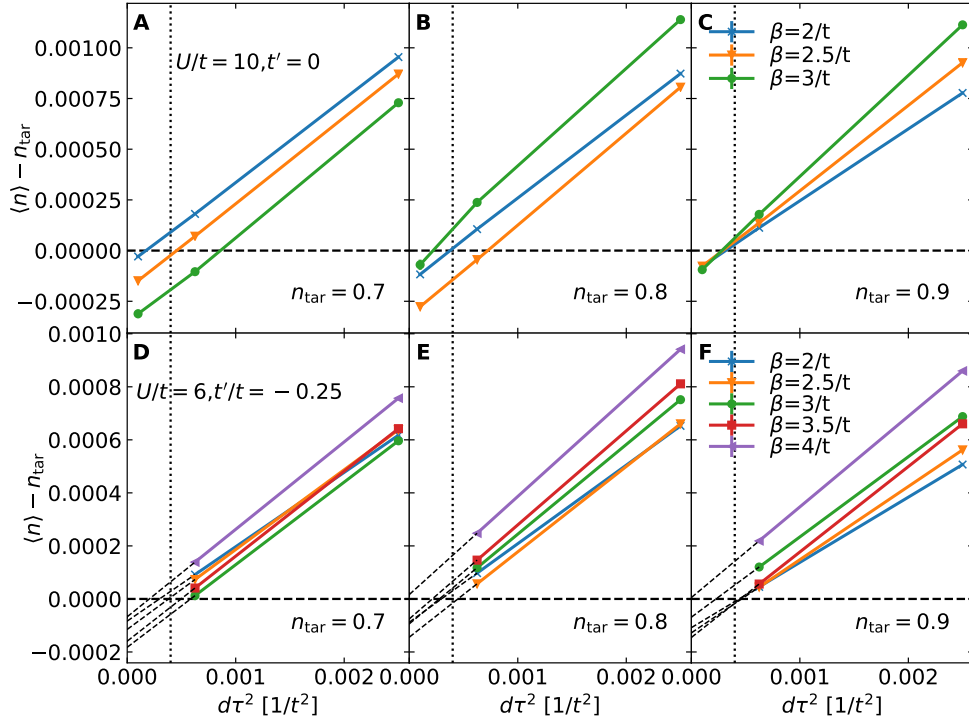


Figure S7: Differences between measured density  $\langle n \rangle$  and target density  $n_{\text{tar}}$  with different  $d\tau$  for (A)-(C)  $U/t = 10, t' = 0$  and (D)-(F)  $U/t = 6, t'/t = -0.25$ , at temperatures indicated in the legend for each row. Vertical dotted lines mark  $d\tau = 0.02/t$ , which is chosen for chemical potential tuning to obtain the chemical potential  $\mu$  corresponding to the target filling  $n_{\text{tar}}$ .  $\mu$  is kept the same for data points on the same curve. Thin dashed lines in (D)-(F) are straight-line extrapolations as a guide for eye. Simulation cluster is  $8 \times 8$ . Error bars are  $\pm 1$  standard error determined by jackknife resampling (smaller than the data points).

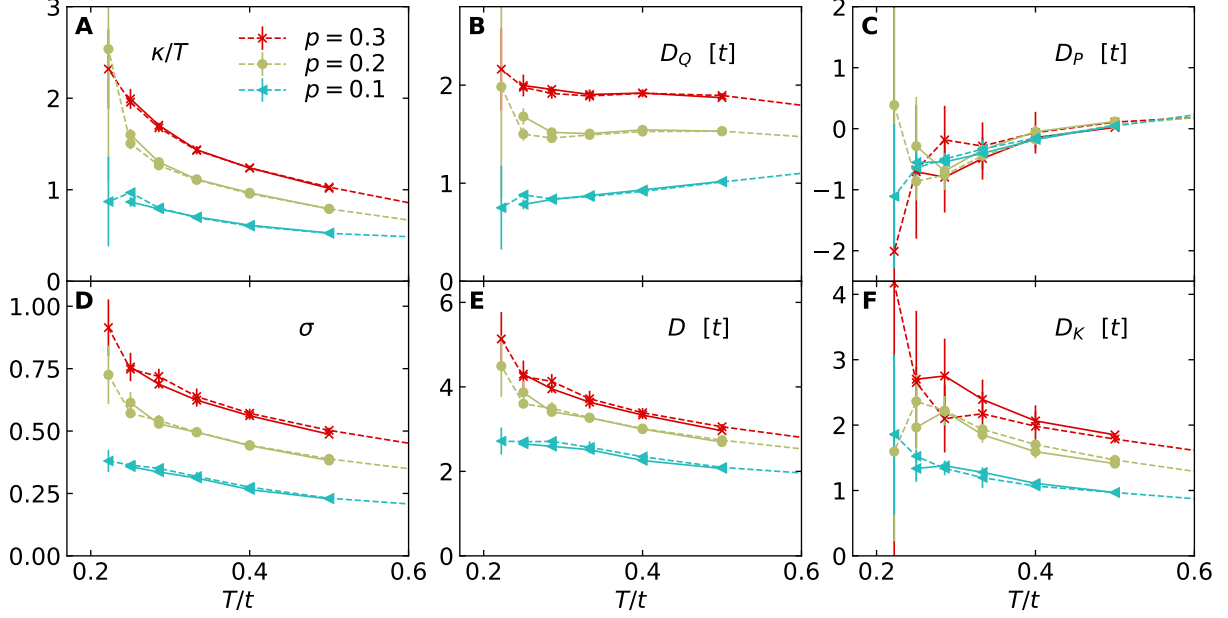


Figure S8: Trotter error analysis for (A)  $\kappa/T$ , (B)  $D_Q$ , (C)  $D_P$ , (D)  $\sigma$ , (E)  $D$ , and (F)  $D_K$ . Dashed lines are for  $d\tau = 0.05/t$  and solid lines are for  $d\tau = 0.025/t$ . The same marker (color) indicates the same doping. Simulation parameters:  $U/t = 6$ ,  $t'/t = -0.25$ , with cluster size  $8 \times 8$ .

$\langle n \rangle - n_{\text{tar}}$  to  $d\tau^2 = 0$  should indicate the “true” value of  $\langle n \rangle(\mu) - n_{\text{tar}}$ . The difference between the actual density  $\langle n \rangle$  at  $\mu$  and the target density  $n_{\text{tar}}$  indicates the tolerance of the density tuning process. Here,  $\mu$  is the chemical potential obtained from tuning with  $d\tau = 0.02/t$ .  $U/t = 10$  is the largest  $U$  considered in this paper, and the deviation  $|\langle n \rangle(\mu) - n_{\text{tar}}|$  is within  $10^{-4}$  as shown in Figs. S7(A)-(C). Since Trotter error should be roughly  $\propto U$  (27), the error  $|\langle n \rangle(\mu) - n_{\text{tar}}|$  for  $U$  smaller than  $10t$  would be expected to fall within the range of  $10^{-4}$  or smaller. As in Figs. S7(D)-(F), lower temperatures are achievable for  $U/t = 6$ ,  $t'/t = -0.25$  than  $U/t = 10$ ,  $t'/t = 0$ , and  $|\langle n \rangle(\mu) - n_{\text{tar}}|$  is still controlled within  $O(10^{-4})$  down to the lowest accessible temperature.

We show the measurement Trotter error in Fig. S8 for  $U/t = 6$ ,  $t'/t = -0.25$  and in Fig. S9 for  $U/t = 10$ ,  $t'/t = 0$ . Results obtained with  $d\tau = 0.05/t$  and  $0.025/t$  show minimal differ-

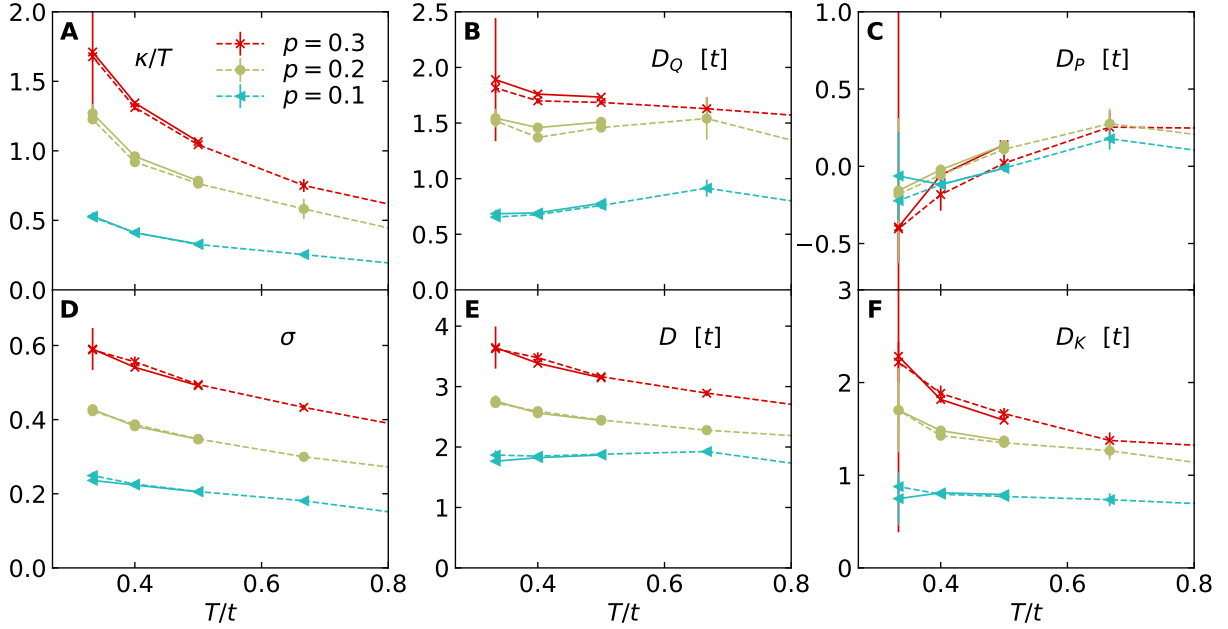


Figure S9: Similar Trotter error analysis as Fig. S8 but for  $U/t = 10$ ,  $t'/t = 0$ .

ence. For transport measurements, in addition to direct changes in the Trotter error, changing  $d\tau$  may affect analytic continuation, as the number of imaginary time points changes for fixed inverse temperature  $\beta$ . Analyzing Figs. S8 and S9, we conclude that  $d\tau = 0.05/t$  is small enough to prevent Trotter error from affecting our conclusions, and it also provides a reasonable value for stable MaxEnt analytic continuation.

### Finite Size Effects Analysis

In Fig. S10, we compare results on  $8 \times 8$  and  $12 \times 12$  clusters with periodic boundary conditions. For  $U/t = 6$ ,  $t'/t = -0.25$ , the differences between the results from the two sizes are minimal and do not affect our conclusions. Higher doping, smaller  $U$ , and lower temperature generally should cause larger finite size effects, as the system becomes more delocalized. This analysis up to 30% doping, with  $U/t = 6$ , and down to the lowest temperatures should represent a worst case scenario for finite-size effects given the parameters considered in this manuscript. We would conclude that for  $U/t = 6 - 10$ , finite size effects should be minimal and would not

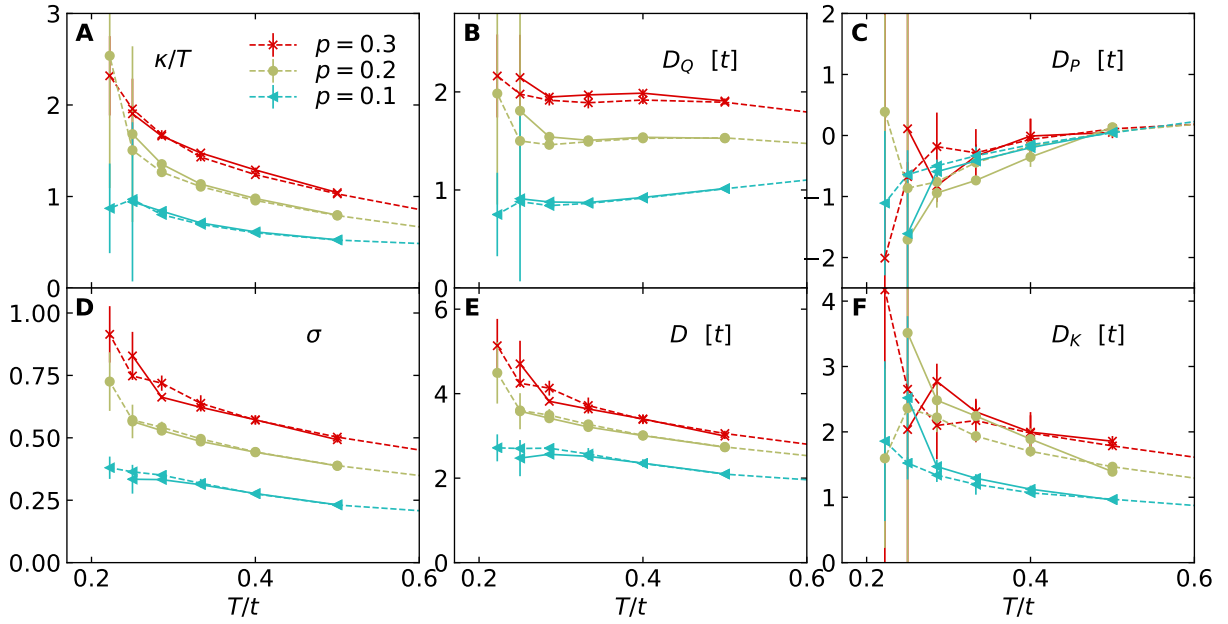


Figure S10: Finite size analysis for (A)  $\kappa/T$ , (B)  $D_Q$ , (C)  $D_P$ , (D)  $\sigma$ , (E)  $D$ , and (F)  $D_K$ . Dashed lines are obtained for simulation clusters of size  $8 \times 8$ . Solid lines are obtained for simulation clusters of size  $12 \times 12$ . Simulation parameters:  $U/t = 6$ ,  $t'/t = -0.25$ ,  $d\tau = 0.05/t$ .

affect our conclusions.